A&A 606, A52 (2017)
DOI: 10.1051/0004-6361/201731056

Astronomy & Astrophysics

First detection of a THz water maser in NGC 7538-IRS1 with SOFIA and new 22 GHz e-MERLIN maps⋆

F. Herpin[1], A. Baudry[1], A. M. S. Richards[2], M. D. Gray[2], N. Schneider[3], K. M. Menten[4], F. Wyrowski[4], S. Bontemps[1], R. Simon[3], and H. Wiesemeyer[4]

[1] Laboratoire d'astrophysique de Bordeaux, Univ. Bordeaux, CNRS, B18N, allée Geoffroy Saint-Hilaire, 33615 Pessac, France
e-mail: fabrice.herpin@u-bordeaux.fr
[2] JBCA, School of Physics and Astronomy, Univ. of Manchester, Oxford Road, M13 9PL, UK,
[3] I. Physik. Institut, University of Cologne, Zülpicher Str. 77, 50937 Cologne, Germany
[4] Max-Planck-Institut für Radioastronomie, Auf dem Hügel 69, 53121 Bonn, Germany

Received 27 April 2017 / Accepted 20 June 2017

ABSTRACT

Context. The formation of massive stars ($M > 10\ M_\odot$, $L > 10^3\ L_\odot$) is still not well understood. Accumulating a large amount of mass infalling within a single entity in spite of radiation pressure is possible if, in addition to several other conditions, enough thermal energy is released. Despite numerous water line observations over a broad range of energies obtained with the *Herschel* Space Observatory, observations were not able to trace the emission from the hot core around the newly forming protostellar object in most of the sources.

Aims. We wish to probe the physical conditions and water abundance in the inner layers of the host protostellar object NGC 7538-IRS1 using a highly excited H_2O line. Water maser models predict that several THz water masers should be detectable in these objects. We therefore aim to detect the o-H_2O $8_{2,7}$–$7_{3,4}$ line in a star forming region for the first time. Model calculations have predicted this line to show maser action.

Methods. We present SOFIA observations of the o-H_2O $8_{2,7}$–$7_{3,4}$ line at 1296.41106 GHz and a 6_{16}–5_{23} 22 GHz e-MERLIN map of the region (the very first 22 GHz images made after the e-MERLIN upgrade). In order to be able to constrain the nature of the emission – thermal or maser – we used near-simultaneous observations of the 22 GHz water maser performed with the Effelsberg radiotelescope and e-MERLIN. A thermal water model using the RATRAN radiative transfer code is presented based on HIFI pointed observations. Molecular water abundances are derived for the hot core.

Results. The o-H_2O $8_{2,7}$–$7_{3,4}$ line is detected toward NGC 7538-IRS1 with one feature at the source velocity (–57.7 km s^{-1}) and another one at –48.4 km s^{-1}. We propose that the emission at the source velocity is consistent with thermal excitation and is excited in the innermost part of the IRS1a, in the closest circumstellar environment of the massive protostellar object. The other emission is very likely the first detection of a water THz maser line, pumped by shocks due to the IRS1b outflow, in a star-forming region. Assuming thermal excitation of the THz line, the water abundance in the hot core of NGC 7538-IRS1 is estimated to be 5.2×10^{-5} with respect to H_2.

Key words. stars: formation – masers – stars: individual: NGC 7538-IRS1 – ISM: molecules – stars: protostars – ISM: abundances

1. Introduction

Massive stars, despite their rarity, are important constituents of galaxies and produce most of their luminosity. The complex and still not clearly defined evolutionary sequence ranges from massive prestellar cores, high-mass protostellar objects (HMPOs), hot molecular cores, and finally to the more evolved ultra compact HII (UCHII) region stage, where the central object begins to ionize the surrounding gas (e.g., Beuther et al. 2007; König et al. 2017). The classification adopted above is of course not unique. The molecular material in star-forming regions has a wide range of temperatures and number densities (10–2000 K and 10^4–10^9 cm^{-3}), with different chemical characteristics. Water is a key molecule for determining the physical and chemical structure of star-forming regions because of the large abundance variations between warm and cold regions. In cool molecular clouds, water is mostly found as ice on dust grains, but at temperatures $T > 100$ K, the ice evaporates, increasing the gas-phase water abundance by several orders of magnitude (Fraser et al. 2001; Aikawa et al. 2008). At temperatures above ~250 K, all gas-phase free oxygen may be driven into H_2O, increasing its abundance to $\sim 3 \times 10^{-4}$ (van Dishoeck et al. 2011).

Major progress in our understanding of interstellar water and star formation has been made with the *Herschel* Space Observatory. The guaranteed-time key program WISH (Water In Star-forming regions with *Herschel*, van Dishoeck et al. 2011) probed massive star-forming regions using water observations. To collapse, the gas must be able to release enough thermal energy, in addition to several other condistions; one main WISH goal was to determine how much of the cooling of the warm regions ($T > 100$ K) is due to H_2O. In particular, the dynamics of the central regions has been characterized using the water lines, and the amount of cooling provided has been measured. *Herschel* observations of many water lines made with the high-spectral resolution Heterodyne Instrument for the Far Infrared (HIFI, de Graauw et al. 2010) allowed observers to perform

⋆ The reduced spectra and maps (FITS files) are only available at the CDS via anonymous ftp to cdsarc.u-strasbg.fr (130.79.128.5) or via
http://cdsarc.u-strasbg.fr/viz-bin/qcat?J/A+A/606/A52

some type of tomography of the whole protostellar environment, and hence to probe the physical conditions and estimate the water abundance from a few 100 AU to a few 10 000 AU from the star (see Herpin et al. 2016). Nevertheless, observational evidence for the water abundance jump close to the forming stars that heats up their environs is still scarce (e.g., van der Tak et al. 2006; Chavarría et al. 2010; Herpin et al. 2012, 2016). While the outer abundance for the HMPOs studied in the WISH program is well constrained and estimated to be a few 10^{-8} in all sources, the inner abundance varies from source to source between 0.2 and 14×10^{-5} (Herpin et al. 2016). Observing water lines involving high enough energy levels will allow us to probe the physical conditions and water abundance in the inner layers of the protostellar environment and thus to address this problem. One main difficulty is that up to now it has been impossible to (i) spatially resolve the region where the water jump occurs and (ii) to probe this region with the help of high-excitation optically thin lines.

Since the end of the *Herschel* mission, only the Stratospheric Observatory for Infrared Astronomy (SOFIA, Young et al. 2012) allows us to observe water in the THz frequency range. Interestingly, some of the THz water lines could even be masing. The H_2O excitation model of Neufeld & Melnick (1991) as well as the works of Yates et al. (1997) and more recently, of Daniel & Cernicharo (2013) and Gray et al. (2016), which incorporated the most recent collisional excitation rates of water with ortho- and para-H_2, all make important predictions of masing transitions in the supra-THz region. Several transitions could be masing that have frequencies within the L1 and L2 channels of the German Receiver for Astronomy at Terahertz Frequencies (GREAT, Heyminck et al. 2012) on board SOFIA (Heyminck et al. 2012). In particular, three predicted o-H_2O masing transitions and one p-H_2O masing transition fall in the 1.25–1.50 THz range. Only one o-H_2O transition, $8_{2,7} - 7_{3,4}$ at 1296.41 GHz, could be observed at the flying altitude of the SOFIA observatory (transmission ≃62%), the others are absorbed by the remaining atmosphere. Emission from this transition involves an upper energy level at 1274.2 K and can probe the gas deep enough into the inner layers of the hot core. We note that Neufeld et al. (2017) have just reported the first detection of the $8_{2,7} - 7_{3,4}$ masing line toward an evolved star.

We have selected NGC 7538-IRS1, the best-studied massive object from our WISH program (Herpin et al. 2016; van der Tak et al. 2013), which has previously been observed in the 22 GHz maser line and exhibits strong thermal water lines. NGC 7538-IRS1 is a relatively nearby (2.65 kpc, Moscadelli et al. 2009) UCHII object in the complex massive star-forming region NGC 7538 surrounded by a molecular hot core. The 22 GHz H_2O masers associated with it exhibit a complex spatial distribution, and the strongest and main concentration of the maser features (see Kameya et al. 1990; Surcis et al. 2011) is found in the direction of IRS1. Until recently (see Beuther et al. 2013), the central source was thought to be an O6 star (30 $M_\odot$, $L \simeq 8\times10^4$ $L_\odot$) forming one single high-mass young stellar object (YSO). New interferometric observations of the methanol masers (Moscadelli & Goddi 2014) have demonstrated that NGC 7538-IRS1 consists of three individual high-mass YSOs named IRS1a, IRS1b, and IRS1c within 1600 AU. We note that IRS1a, b, and c are associated with the methanol maser clusters labeled by Minier et al. (2000) B+C, A, and E, respectively. The most massive YSO is IRS1a, with ∼25 $M_\odot$ and a quasi-Keplerian disk of ∼1 $M_\odot$ that dominates the bolometric luminosity of the region. Another massive (≤16 $M_\odot$) and thick disk orbits the less massive (a few $M_\odot$) IRS1b object. The third source, IRS1c, is likely to be a massive YSO as well.

Several bipolar outflows or jets emanating from the IRS1 region in multiple directions have been identified and characterized. A north-south free-free ionized jet with an opening angle ≤30° has been observed by Sandell et al. (2009), as well as a strong accretion flow toward IRS1 ($\dot{M} \sim 2 \times 10^{-3}$ $M_\odot$/yr). Several studies have characterized the NW-SE (PA = −50°, Qiu et al. 2011) CO outflow now thought to originate from IRS1a (Moscadelli & Goddi 2014). In addition, a NE-SW outflow with PA = 40° has been observed by Beuther et al. (2013). An outflow driven by IRS1b that is collimated by its rotating disk has also been observed (Moscadelli & Goddi 2014). The presence of jets or outflows and strong accretion flows makes this shocked region an ideal place for exciting masers.

In this paper we report an observational study of the NGC 7538-IRS1 region. The o-H_2O $8_{2,7}-7_{3,4}$ emission was observed with the GREAT instrument on board SOFIA. In addition, the 22 GHz water maser emission was observed using the Effelsberg telescope and the e-MERLIN interferometer. In Sect. 2 we describe the observations, and we present the observational data in Sect. 3. In Sect. 4 we discuss the nature of the detected THz water emission. In Sect. 5 we discuss the region kinematics and physical conditions, and in Sect. 6 we summarize the results of our study.

2. Observations and data reduction

2.1. SOFIA observations

Observations in single-point chopping mode of the $8_{2,7}-7_{3,4}$ line of ortho-$H_2^{16}O$ were carried out toward NGC 7538-IRS1 ($\alpha_{J2000} = 23^h13^m45.3^s, \delta_{J2000} = +61°28'10.0''$) as part of the SOFIA Cycle 3 project on 2015 December 9, using GREAT. At the systemic velocity of NGC 7538-IRS1, the system temperature was typically 2000 K (SSB) and signal-band zenith opacity 0.08. The on-source integration time was 20 min. The chop throw was 100″ to either side of the on-source position (chop-nod method). One channel (L1) of GREAT was tuned to the 1296.41106 GHz water line frequency (lower sideband LSB), the other channel, the Low Frequency Array (LFA) seven-pixel array, was tuned to the [CII] 158 μm line. The [CII] line was detected but a discussion of these results will be presented elsewhere. We employed the digital 4GFFT spectrometer (Klein et al. 2012) that analyzed a bandwidth of 1.5 GHz with a spectral resolution of 0.283 MHz (0.056 km s^{-1}). Data have later been smoothed to 1.129 km s^{-1}. The rms of the spectra is 90 mK at this latter spectral resolution.

The data were processed with the latest version of the GREAT calibrator and converted from the T_A^* scale (η_f = 0.97) into main-beam temperature units, T_{MB}, by applying the main-beam coupling efficiency η_{mb} = 0.69 for the L1 channel. The conversion factor Jy/K we applied on the T_A^* data is 971 Jy/K. The half-power beam width is 20.6″ at this frequency. All spectra were calibrated for the transmission in the signal band, and the continuum-level correction for double-sideband reception was applied. Further analysis was made within the CLASS[1] package. The continuum level (SSB) is T_{MB} = 2.0 K (at 1296.4 GHz).

2.2. Effelsberg observations

In order to constrain the maser models and because of the variability of the maser emission, nearly contemporaneous

[1] http://www.iram.fr/IRAMFR/GILDAS/

observations of the 6_{16}–5_{23} transition of ortho-H_2O (rest frequency 22.23508 GHz) were carried out on 2015 December 11 (integration time on-source of 15 min) with the MPIfR 100 m telescope at Effelsberg, Germany. The half-power beam width was $\simeq 39''$ and the pointing accuracy was, on average, $4''$. We used the 1.3 cm double-beam secondary focus receiver (K/Jy conversion factor of 1.6) with the XFFT backend in high-resolution mode (32768 channels with a spectral resolution of $\sim$0.04 km s^{-1}). Data were smoothed to 0.1 km s^{-1} and the rms noise at this resolution is 37 mJy. The system temperature was 190 K. All data were calibrated in Jy; the calibration parameters were derived by continuum observations of suitable flux density calibrators. The main-beam efficiency is 0.64. The calibration uncertainty is about 10–15%.

2.3. e-MERLIN observations

Interferometric observations of the same source of the ortho-H_2O 6_{16}–5_{23} line emission were performed with e-MERLIN (commissioning observations) on 2016 April 20. These were the very first 22 GHz images made after the e-MERLIN upgrade. Four telescopes were used, the longest baseline being 217 km, with the 25 m Mark 2, Darnhall, and Pickmere telescopes and the 32 m Cambridge telescope. At the assumed distance of 2.7 kpc, the synthesized beam of 20 mas corresponds to a spatial resolution element of approximately 54 AU, but the positions of individual bright maser components can be fit with a relative accuracy $\sim$1 AU.

The observations were made in full Stokes parameters (although only the parallel bands were processed, giving total intensity images). One spectral window (spw) of 4 MHz was centered on the 22.23508 GHz maser line (adjusted for the source velocity immediately before observations), divided into 512 channels, giving a spectral resolution of 0.105 km s^{-1} and a total useful span $\sim$50 km s^{-1}. Two similar spw were placed either side (but they did not contain any emission). A single 125 MHz spectral window (also with 512 channels) was placed to overlap them for calibration. The pointing position of $\alpha_{J2000} = 23^h14^m01.749^s, \delta_{J2000} = +61°27'19.80''$ was used for NGC 7538, which was approximately observed 10 h on target, in 6-min scans interleaved with the phase reference source J2302+6405. The quasar 3C 84 was used to provide the bandpass correction and flux scale, with a flux density in 2016 April of 37 Jy (measurements kindly provided by Anne Lähteenmäki, Metsahovi, priv. comm.). The local standard of rest (LSR) correction was applied to the line data before self-calibration and imaging.

The calibration was performed in CASA, and final imaging and component fitting in AIPS. The position of the brightest maser was established as a reference position before self-calibration. Test image cubes were made at coarse resolution to look for masers within $\sim$1.5 arcmin radius of the pointing center (within the half-power point of the primary beam). Four fields were imaged at full resolution, covering all the emission we identified, see Table 1.

The e-MERLIN beam at 22 GHz is not yet fully characterized. We made images without primary beam correction, and then fit 2D Gaussian components to each patch of emission above $4\sigma_{rms}$ (rejecting components that were isolated in fewer than three channels or any obvious sidelobes of brighter components). We estimated the primary beam corrections using a scaled VLA beam, and divided the measured fluxes by the factors given in Table 1, with uncertainties increasing with distance from the pointing center. The most distant fields were also slightly affected (<10%) by time smearing.

The noise σ_{rms} is $\sim$20 mJy in quiet channels for fields close to the pointing center (IRS 1–3), rising to twice that in the most distant fields. The sparse visibility plane coverage means that the brighter channels are severely dynamic-range limited, with σ_{rms} typically 10% of peaks, or even more in more remote fields. The astrometric position accuracy is a few tens of milliarcseconds (mas); the relative accuracy depends on the signal to noise ratio and is <1 mas for all but the faintest or most remote components.

2.4. HIFI observations

The source NGC 7538-IRS1 was part of the WISH GT-KP sample. Fifteen water lines (see Table A.1) were observed with the HIFI spectrometer on board the *Herschel* Space Observatory in the pointed (or mapping) mode at frequencies of between 547 and 1670 GHz in 2010 and 2011 (the observation identification numbers, *obsids*, are listed in Table A.1) toward NGC 7538-IRS1 (same coordinates as for SOFIA observations). For the pointed observations, the double-beam switch observing mode with a throw of 3′ was used. The off positions were inspected and do not show any emission. The frequencies, energy of the upper levels, system temperatures, integration times, and rms noise levels at a given spectral resolution for each of the lines are provided in Table A.1.

Data were taken simultaneously in H and V polarizations using both the acousto-optical Wide-Band Spectrometer (WBS) with 1.1 MHz resolution and the digital autocorrelator or High-Resolution Spectrometer (HRS). Calibration of the raw data into the T_A scale was performed by the in-orbit system (Roelfsema et al. 2012). Conversion into T_{mb} was made using the beam efficiency[2] given in Table A.1 and a forward efficiency of 0.96. The flux scale accuracy is estimated to be between 10% for bands 1 and 2, 15% for bands 3 and 4, and 20 % in bands 6 and 7[1]. Data calibration was performed in the *Herschel* Interactive Processing Environment (HIPE, Ott 2010) version 14. Further analysis was made within CLASS. These lines are not expected to be polarized. Thus, after inspection, data from the two polarizations were averaged together. Because HIFI is operating in double-sideband mode, the measured continuum level was divided by a factor of 2 in the figures and tables (this is justified because the sideband gain ratio is close to 1). We note that the p-H_2O 5_{24}–4_{31} line is affected by strong baseline and ripple problems.

3. Analysis

3.1. THz water emission

The ortho-$H_2^{16}O$ $8_{2,7}$–$7_{3,4}$ line emission is detected toward NGC 7538-IRS1 with SOFIA. As shown in Fig. 1, the line profile exhibits two features at -57.7 ± 0.6 and -48.4 ± 0.5 km s^{-1} where 22 GHz emission is also observed (see Fig. 2). From Gaussian fitting, the S/N ratio of the integrated lines at –57.7 and –48.4 km s^{-1} is 5.5 and 3.2, respectively. Hereafter the –57.7 and –48.4 components are called features (1) and (2), respectively. At the frequency of the observed emissions, there is no contamination by other molecular species according to *Splatalogue* catalog[3]. The peak intensities and line widths are

[2] http://herschel.esac.esa.int/twiki/pub/Sandbox/TestHifiInfoPage/

[3] http://www.cv.nrao.edu/php/splat/

Table 1. e-MERLIN 22 GHz imaging parameters.

Field	RA, Dec (J2000) hh:mm:ss dd:mm:ss	Size ″	Flux error %	PB correction divisor
New	23:13:43.69442 +61:27:49.3597	6	6	0.95
IRS11	23:13:44.98183 +61:26:49.6800	6	10	0.88
IRS1-3	23:13:45.14200 +61:28:11.4100	12	5	1.0
IRS9	23:14:01.75100 +61:27:19.8000	6	15	0.8

Notes. The table includes: center of the square field, length of the side, fractional error in flux scale, and primary beam (PB) correction.

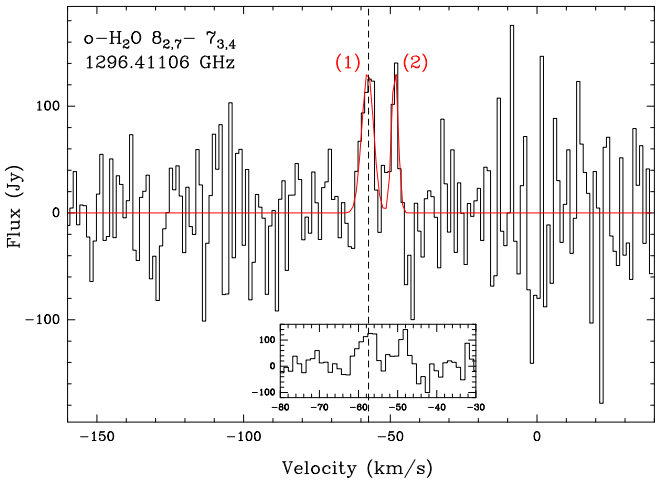

Fig. 1. Continuum-subtracted SOFIA spectra of the o-H_2O $8_{2,7}$−$7_{3,4}$ line at 1296.41106 GHz toward NGC 7538-IRS1. The vertical dotted line indicates V_{LSR} at –57.4 km s^{-1}. The spectral resolution is 1.129 km s^{-1}. The Gaussian fit is shown in red. The small insert shows the same spectra on a zoomed velocity scale.

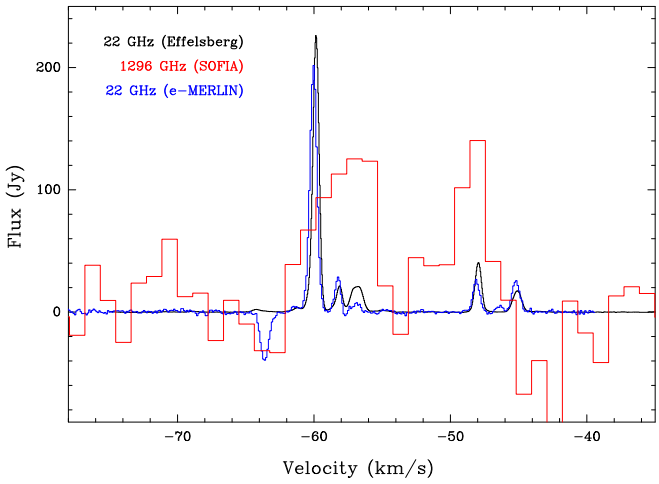

Fig. 2. Effelsberg (in black, spectral resolution δv of 0.1 km s^{-1}) and e-Merlin (in blue, δv = 0.1 km s^{-1}, the apparent absorption near –63.5 km s^{-1} is attributed to e-MERLIN residual sidelobes, see Sect. 3.3) spectra of the 6_{16}−5_{23} transition of ortho-H_2O at 22 GHz toward NGC 7538-IRS1 plotted over the SOFIA (δv = 1.1 km s^{-1}) spectrum of the o-H_2O $8_{2,7}$−$7_{3,4}$ line at 1296.41106 GHz (in red).

133.1 Jy and 4.7 (±1.3) km s^{-1} for feature (1), and 139.4 Jy and 2.6 (±1.3) km s^{-1} for feature (2).

The velocity and line width of feature (1) are comparable to what has been observed from the CS thermal lines (v_{LSR} = −57.4 km s^{-1}, δv = 5.5 ± 1 km s^{-1}, van der Tak et al. 2000) or OH with SOFIA (Csengeri et al. 2012). Conversely, feature (2) is centered at a velocity different from the generally adopted source velocity. In addition, the line is narrower by a factor of 2. The nature of these water components is discussed in Sect. 4.

3.2. 22 GHz single-dish observation

Several velocity components of the 22 GHz water maser line are seen in the Effelsberg spectra (see Fig. 2). All lines are narrow with a width on the order of 1 km s^{-1} or less. Two main groups of lines can be distinguished: one made of three strong lines close to the source velocity (∼−(56−60) km s^{-1})), and another group with two lines centered at –45.1 and –48 km s^{-1}. These lines are highly variable with time (on a timescale of several months), as shown by Felli et al. (2007) from their long-term monitoring observations. Nevertheless, most of the time, the ∼−60 km s^{-1} feature is the strongest maser line.

According to the existing 22 GHz maser maps and our e-MERLIN map (see next section), all of these maser components are associated with IRS1-3. The non-detections of more distant masers are explained by the Effelsberg telescope's primary beam, which is smaller by one-third than that of e-MERLIN.

3.3. Map of the 22 GHz maser emission

The entire e-MERLIN map, shown in Fig. 3, encompasses the highly luminous infrared sources IRS1-3, IRS9, and IRS11 which were first identified by Werner et al. (1979). We have identified 286 individual features that can be gathered into 109 groups based on their peak velocity and coordinates. All these groups are reported in Table B.1, where their position, peak flux density S_ν, peak velocity, and velocity range are listed. We have compared our maser positions with the work of Galván-Madrid et al. (2010), taking into account the proper motions from Moscadelli & Goddi (2014), μ_{RA} = −2.45 mas/yr and μ_{Dec} = −2.45 mas/yr. Both maps are consistent. Our Figs. 3 and 4 around IRS1-3 and IRS11 show maser positions very close to those labeled M and S in Table 2 of Galván-Madrid et al. (2010) and are shown here as green crosses. Moreover, the total size of the image around IRS1-3 (12″, a size comparable to the SOFIA beam at 1.3 THz) was used to synthesize the e-MERLIN 22 GHz spectrum, which we compare in Fig. 2 with the line profile obtained at Effelsberg in order to verify the flux density scale (e-MERLIN data are commissioning data), and to check that the interferometer is detecting the entire flux. Both line profiles are very similar, except for the apparently negative feature in the –63.5 to –64 km s^{-1} velocity range, which is due to residual sidelobes arising from strong IRS11 emission in this velocity range. The maser variability over this short time-period (four months) is thus not significant and the entire flux is detected.

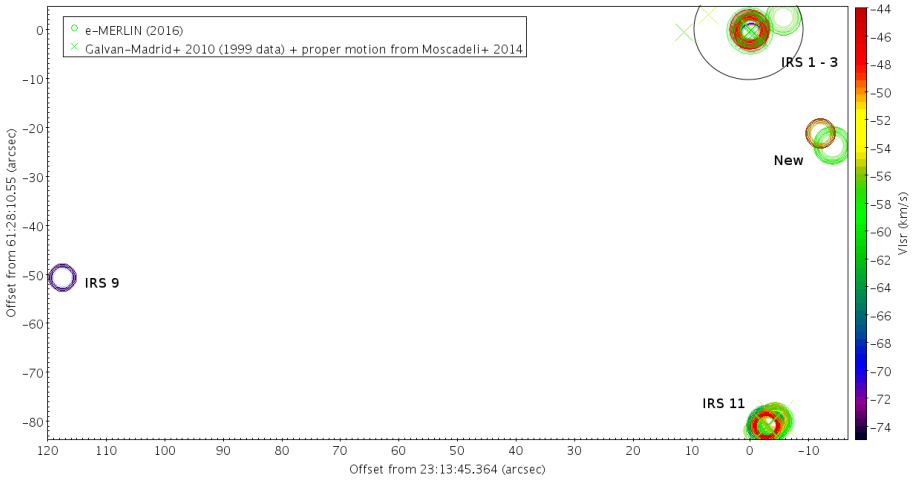

Fig. 3. Entire e-MERLIN map of 22 GHz maser emission from NGC 7538, including IRS1-3, IRS9, and IRS11, of the 22 GHz water maser line. Colored circles show the relative position of individual maser features, with color denoting the maser $V_{\rm LSR}$, according to the color-velocity conversion code reported on the right side of the panel. The water maser positions reported by Galván-Madrid et al. (2010), corrected for proper motion (Moscadelli & Goddi 2014), are shown as crosses (same color-velocity conversion code) for comparison. The beam of the SOFIA observation is overlaid in black for comparison.

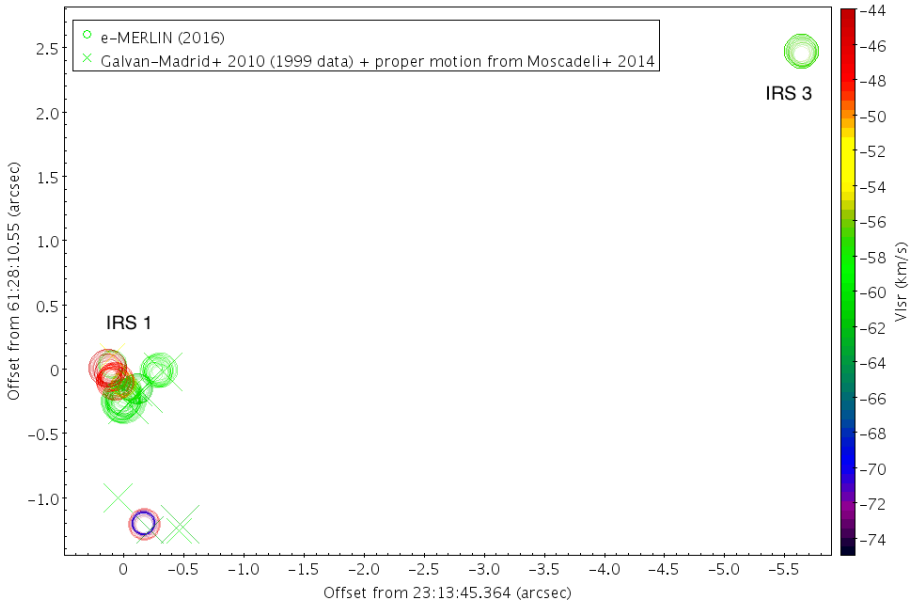

Fig. 4. As in Fig. 3, but zoomed on IRS1-3.

We detect 68 maser groups for IRS11, some of them very bright with S_ν well above 100 Jy, spanning a velocity range from –44.75 to –65.08 km s^{-1}. The maximum flux is observed at –60 km s^{-1} (964 Jy) in IRS1. Only three main groups of masers are observed toward IRS9, and they are blueshifted ($\sim$–(69–79) km s^{-1}) compared to IRS1 source velocity. The strongest maser group peaks at 39 Jy in IRS9.

Approximately 25 arcsec southwest from IRS1 (offsets $\sim$–(12–14)″ and –(21–24)″), a new source has been found that exhibits powerful maser emission (up to $\sim$200 Jy for group 5) and velocities from –45 to –63 km s^{-1} (see Fig. 3 and Table B.1). The feature "E" observed by Kameya et al. (1990) with $V_{\rm LSR}$ = −63.3 km s^{-1} at $\alpha_{\rm J2000}$ = 23$^{\rm h}$13$^{\rm m}$42.51$^{\rm s}$, $\delta_{\rm J2000}$ = +61°27′45.1″, that is at offset $\sim$−20″ and −25″, is much farther away from this new spot.

A first zoom of the IRS1-3 region is shown in Fig. 4. The IRS3 source lies to the NW with offsets from IRS1 of –5.5″ and 2.5″ in RA–Dec, respectively. Two main groups are detected for IRS3, they are moderately bright (14–88 Jy) and span a small velocity range (from $\sim$–56 to –58 km s^{-1}). At this scale, IRS1 is made of what Surcis et al. (2011) called the *north source* (the main source) and the *nouth* source, 1.2″ south. In addition to the maser group at $\sim$−70 km s^{-1} for IRS1, which has also been observed by these authors, we detect maser spots at redder velocities of $\sim$−46 km s^{-1}.

The close-up view of $H_2^{16}O$ maser features around NGC 7538-IRS1 North (see Fig. 5) reveals 26 maser groups that can be split into two distinct velocity ranges: a first large group of masers within ±3 km s^{-1} from the main source LSR velocity, represented in blue in Fig. 5, and a second group of redshifted masers whose LSR velocity is between –45 and –48 km s^{-1}. The "blue" group is made of numbers of features that are concentrated very close to IRS1a (as defined by Moscadelli & Goddi 2014) plus several spots spread in the northwest. The "red" group masers lying north of IRS1a are less well aligned along a NE–SW direction. The maser spatial distribution is discussed in more detail in Sect. 4.1.

4. Nature of the THz water emission

4.1. Spatial origin

Considering the SOFIA beam size (≃21″) and the approximate 12″ square size of the image made by e-MERLIN (primary beam, see Table 1) toward IRS1-3 (see Figs. 3 and 4), the detected THz water emission can only originate from IRS1-3. Then, comparing the velocity range of features (1) and (2) with

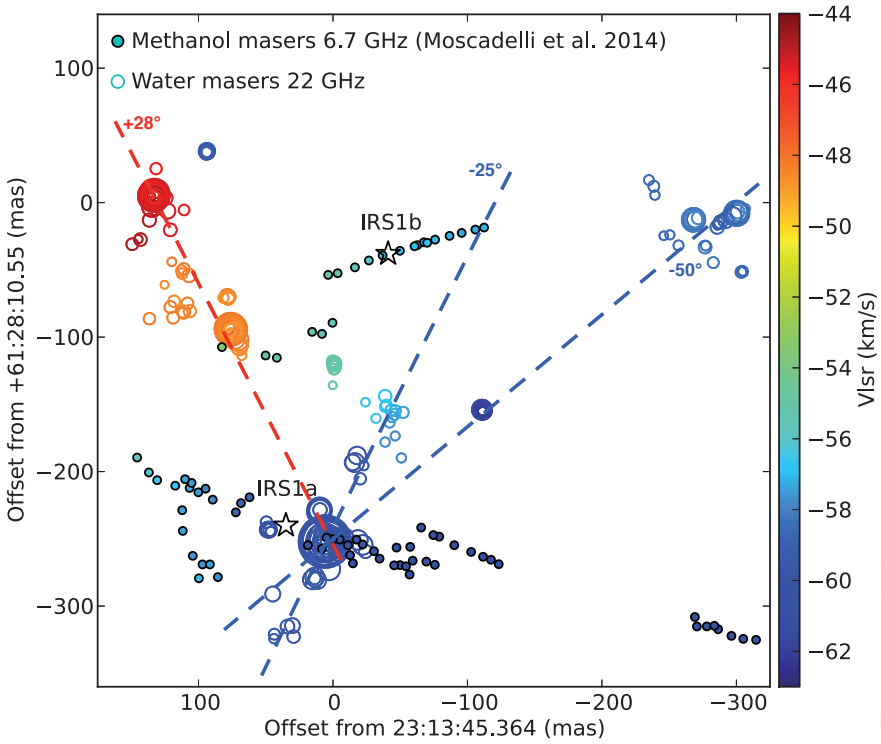

Fig. 5. Zoom toward IRS1 north of the e-MERLIN map shown in Fig. 3. Colored empty and filled circles show the relative position of individual 22 GHz water masers (this paper) and 6.7 GHz methanol maser features (Moscadelli & Goddi 2014), respectively. V_{LSR} is according to the color-velocity conversion code shown on the right side of the panel.

the velocity of maser spots detected by e-MERLIN (Figs. 2 and 4 and Table B.1), we can infer the following:

- water in IRS1 North or IRS3 can give rise to feature (1),
- only IRS1 North exhibits 22 GHz maser emission at velocities (∼−48.4 km s^{-1}) similar to feature (2) THz emission.

At the scale of Fig. 5, we can see that the sizes of the respective emitting regions for maser features around –48 and –58 km s^{-1} are comparable, but not spatially coincident. Maser spots at velocities similar to THz feature (2) emission are located 0.2″ northeast of the high-mass YSO IRS1a and even more than 0.1″ east of the massive protostar IRS1b. We also conclude that a similar beam dilution of the two maser features is obtained with the Effelsberg 22 GHz beam (≃39″).

4.2. Thermal or maser?

4.2.1. Thermal modeling

All water lines observed toward NGC 7538-IRS1 with HIFI are shown in Fig. 6. A detailed analysis of three low-J $H_2^{16}O$ line profiles has been made by van der Tak et al. (2013) in several HMPOs, including NGC 7538-IRS1. Several lines from the rare isotopologue $H_2^{18}O$ and the para-ground-state line of $H_2^{17}O$ were detected in addition to the $H_2^{16}O$ lines toward NGC 7538-IRS1 (see Fig. 6, left).

A Gaussian fit to these line profiles (see Table 2) indicates, depending on the line, three velocity components: a narrow (3.2–4.6 km s^{-1}), a medium (5.1–9.3 km s^{-1}), and a broad (>12.2 km s^{-1}) velocity component. The physical origin of these components (attributed to a dense core, an envelope, and an outflow) has been discussed in several papers (e.g., Herpin et al. 2016). All of these components in NGC 7538-IRS1 are globally centered at a velocity similar to that of the THz feature (1), that is, ∼−57 km s^{-1}. No emission is detected at –48 km s^{-1}, which is thus a first indication of the nonthermal origin of this emission.

Following the method of Herpin et al. (2012, 2016), we modeled all water line profiles in a single spherically symmetrical model using the 1D radiative transfer code RATRAN (Hogerheijde & van der Tak 2000). The envelope temperature (20–1130 K) and number density (1.1×10^5–3.8×10^8 cm^{-3}) structure for the hot core is taken from van der Tak et al. (2013). This analysis assumes a single source within the HIFI beam, hence encompassing the IRS1-3 substructure. The outflow parameters, intensity and width, come from our Gaussian fit (see Table 2) for the broad component. The envelope contribution is parametrized with the water abundance (outer χ_{out} for $T <$ 100 K, inner χ_{in} for $T >$ 100 K, assuming a jump in the abundance in the inner envelope at 100 K due to the evaporation of ice mantles), the turbulent velocity (v_{turb}), and the infall velocity (v_{inf}). We adopt the following standard abundance ratios for all the lines: 4.5 for $H_2^{18}O/H_2^{17}O$ (Thomas & Fuller 2008), 614 for $H_2^{16}O/H_2^{18}O$ (based on Wilson & Rood 1994), and 3 for ortho/para H_2O.

Considering that the width of the velocity components is not the same for all lines (see Table 2), a model with an equally turbulent velocity for all lines does not fit the data well. The best result (see Fig. 6) is obtained with a turbulent velocity of 1.5–2.5 km s^{-1} (5.5 km s^{-1} is even needed for the doubtful p-H_2O 5_{24}–4_{31} line) for $H_2^{16}O$, depending on the modeled line, and 2.5 km s^{-1} for the rare isotopologues lines. No infall is needed at the scale probed by the HIFI lines. All modeled lines are centered at roughly −57.4 ± 0.5 km s^{-1}.

Modeling of the entire set of observed lines constrains the water abundance, but only a few lines are optically thin enough to probe the inner part of the envelope. We hence derive $H_2^{16}O$ abundances relative to H_2 of 8×10^{-6} in the inner part and of 2×10^{-8} in the outer part.

We then applied the results of the above thermal model to feature (1) of the THz o-H_2O $8_{2,7}$–$7_{3,4}$ line (we do not see any thermal line corresponding to feature 2), assuming the same abundance and v_{turb} = 2.5 km s^{-1}. Figure 7 shows that we do not reproduce the observed line, the intensity being only half

Table 2. Observed line emission parameters for the detected lines with HIFI toward NGC 7538-IRS1.

Line	T_{mb} [K]	T_{cont} [K]	v_{nar} [km s^{-1}]	Δv_{nar} [km s^{-1}]	v_{med} [km s^{-1}]	Δv_{med} [km s^{-1}]	v_{br} [km s^{-1}]	Δv_{br} [km s^{-1}]	τ
o-$H_2^{18}O$ 1_{10}–1_{01}	0.63	0.5			–58.4 ± 0.4	5.2 ± 1.1			
p-$H_2^{18}O$ 2_{02}–1_{11}	1.90	1.7	–59.5 ± 0.2	3.9 ± 0.5					
o-$H_2^{18}O$ 3_{12}–3_{03}	2.27	2.0			–58.2 ± 0.2	5.1 ± 0.3			
p-$H_2^{18}O$ 1_{11}–0_{00}	2.22	2.0			–57.7/–64.3[a] ± 0.2	5.1/8.8 ± 0.2			0.03
p-$H_2^{17}O$ 1_{11}–0_{00}	1.9	2.0	–56.7 ± 0.3[a]	3.2 ± 0.6					0.04
o-H_2O 1_{10}–1_{01}	5.21	0.5	–57.1[a]/–54.7[a] ± 0.2	2.0/3.9 ± 0.2			–57.2 ± 0.2	13.0 ± 0.3	0.9
p-H_2O 2_{11}–2_{02}	6.86	0.8	–57.5 ± 0.1	4.3 ± 0.1			–57.6 ± 0.1	15.2 ± 0.3	
p-H_2O 5_{24}–4_{31}[b]	1.75	1.6					–57.6 ± 0.7	12.2 ± 1.6	
p-H_2O 2_{02}–1_{11}	7.92	1.6	–57.4 ± 0.1	4.4 ± 0.1			–57.7 ± 0.1	12.3 ± 0.3	
o-H_2O 3_{12}–3_{03}	6.32	2.0	–57.3 ± 0.1	3.4 ± 0.1	–57.8 ± 0.1	8.5 ± 0.2			
p-H_2O 1_{11}–0_{00}[c]	0.1	2.0	–56.1 ± 0.4[a]	4.6 ± 0.1	–51.2 ± 0.4[a]	9.3 ± 0.6	–55.8 ± 0.2	24.0 ± 0.4	2.9
o-H_2O 2_{21}–2_{12}	5.9	4.0[d]			–60.6[a]/–56.3 ± 0.3	5.1/8.7 ± 0.5			0.4
o-H_2O 2_{12}–1_{01}	0.0	4.0[d]			–58.2[a]/–52.1 ± 0.3	5.7/8.1 ± 0.5			>7

Notes. T_{mb} is the peak temperature with continuum. T_{cont} is the real continuum temperature (single sideband). v is the Gaussian component peak velocity. Δv is the velocity full-width at half-maximum (FWHM) of the narrow, medium, and broad components. The opacity τ is from absorption lines. [(a)] In absorption; [(b)] line suffering from strong baseline and ripples problems; [(c)] WBS data; [(d)] the continuum level is not reliable.

what is observed. We can perfectly reproduce feature (1) with an increased water inner abundance of 5.2×10^{-5} (see blue line in Fig. 7). We also successfully applied this new model to the $H_2^{18}O$ 3_{13}–2_{20} line ($E_{up} \simeq 200$ K), reproducing the line intensity and width observed by van der Tak et al. (2006).

Adopting now the water inner abundance deduced from our modeling of the o-H_2O $8_{2,7}$–$7_{3,4}$ line, we again modeled the HIFI water thermal lines (in blue in Fig. 6). The result is less satisfactory, especially for the p-H_2O 5_{24}–4_{31} (but this observation is affected by line ripples, and the baseline determination is also affected by methanol line blending) and rare isotopologue lines. This might reflect the limitations of our symmetrical 1D model. It is also possible that the $8_{2,7}$–$7_{3,4}$ line detected by SOFIA emanates from the inner part of the hot core, while the water lines observed with HIFI are from somewhat cooler regions farther out. Thus, a temperature gradient could explain our results without requiring a higher water abundance throughout the region. On the other hand, feature (1) of the 1296 GHz water line and the $H_2^{18}O$ 3_{13}–2_{20} line can be well matched by a thermal emission profile if the water abundance is increased. Nevertheless, nonthermal effects cannot be excluded: our RATRAN model could miss a nonthermal contribution at 1296 GHz, which, in that case, would be on the order of 50%.

4.2.2. Maser modeling

We have made quasi-contemporaneous observations of the potentially masing o-H_2O $8_{2,7}$–$7_{3,4}$ transition at 1296 GHz and of the 22 GHz maser line to provide line intensity ratios enabling us to estimate the physical conditions leading to these maser emissions. Line intensity ratios are less dependent on the cloud geometry, and in the saturated regime, such ratios tend to be independent of the exact ratio of the beaming angles, which should then be close to one.

We estimate the 1296/22 opacity ratio from the recently published models of Gray et al. (2016). These models incorporate 411 levels and 7597 radiative transitions, the most recent collision rates, and line overlap effects. Even if these models have been developed primarily for evolved stars, the broad physical parameter space (including T_{dust} rising from 50 K to 350 K) that has been explored can be used for the conditions considered here. There is a significant overlap between conditions supporting the 22 GHz and 1296 GHz masers, for instance, both could come from gas above 1000 K with o-H_2O number densities between 10^4 and 2×10^5 cm^{-3} (i.e., $n_{H_2} \sim 3 \times 10^9$–$6 \times 10^{10}$ cm^{-3}, taking 3×10^{-5} as standard conversion factor from $n(H_2O)$ to $n(H_2)$, Gray et al. 2016). However, strong 1296 GHz maser emission is obtained for a relatively narrow range of physical conditions, typically T_K around 1000 to 3000 K and n_{H_2O} around 10^4–10^5 cm^{-3}, while 22 GHz masers are excited within 500 to 3000 K and for a broader range of H_2O densities up to several 10^5 cm^{-3}. Compared to the 22 GHz inversion, the 1296 GHz inversion is biased toward higher values of T_K and it is lost with increasing dust temperatures, namely a low value of T_{dust}, around 50 K, is preferred. The dust temperature is unlikely to be much higher than 50 K in shocked gas. Assuming $T_{dust} = 50$ K, Gray et al. (2016) predicted $\tau(1296)/\tau(22) \sim 1.9$. This ratio does not result from specific conditions representing the observed source. It is, instead, the ratio of the maximum 1296 GHz depth to the maximum found at 22 GHz from models covering a large parameter space. Saturation is also not accounted for in this ratio. Nevertheless, the 1.9 ratio suggests that the flux density and brightness temperature at 1296 GHz can be several times that at 22 GHz. To compare features (1) and (2) to our model predictions, we derive the line peak ratios from Fig. 8 where all spectra have been smoothed to the same spectral resolution. We derive S(1296)/S(22) = 1.2 and 7.4 for features (1) and (2), respectively, but cannot directly estimate the brightness temperature of the 1296 GHz emission since its spatial extent is unknown. At –48 km s^{-1}, feature (2) is definitely much brighter in the 1296 GHz line than at 22 GHz. This is in agreement with maser conditions suggested from the 1.9 opacity ratio above. We further note that feature (2) is nearly 2.5 times narrower than feature (1) suggesting again that the former is not thermal. Assuming that the 1296 and 22 GHz emissions have a similar spatial extent, we derive from the observed S(1296)/S(22) = 7.4 at –48 km s^{-1}, $T_b(1296) = T_b(22) \times 2.2 \times 10^{-3}$ and, because the condition $T_b(22)$ on the order of or greater than 10^6 K is easily met at 22 GHz (e.g., Elitzur et al. 1992), we get $T_b(1296)$ greater than 2200 K, that is, suprathermal emission. We stress

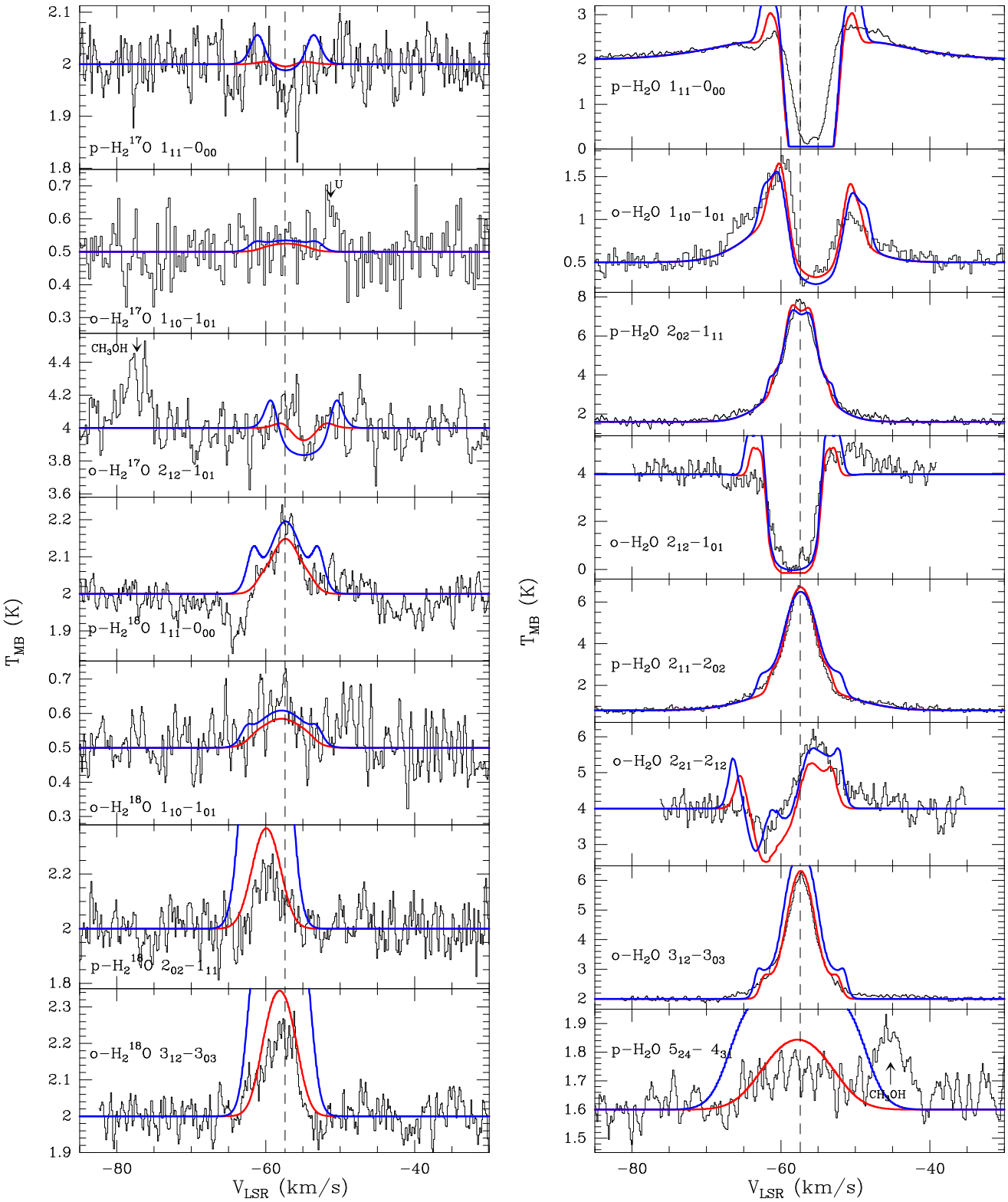

Fig. 6. HIFI spectra of $H_2^{17}O/H_2^{18}O$ (*left*) and $H_2^{16}O$ (*right*) lines (in black), with the continuum for NGC 7538-IRS1 pointed position. The best-fit model is shown as a red line over the spectra ($\chi_{in}(H_2O) = 8\times10^{-6}$ and $\chi_{out}(H_2O) = 4\times10^{-8}$). The model adopting the SOFIA water inner abundance (5.2×10^{-5}) is shown as a blue line above the spectra. Vertical dotted lines indicate the V_{LSR} (–57.4 km s^{-1} from the line modeling). The spectra have been smoothed to 0.2 km s^{-1}, and the continuum is divided by a factor of two.

that deriving an exact value for $T_b(1296)$ is impossible since we have no spatial information. When we use the e-MERLIN resolution of 20 mas as an upper limit to the beamed size of maser spots, however, we obtain T_b in the range $>10^6$ to $>10^9$ K, with a mean value of $>3 \times 10^7$ K. The beamed area of maser spots is likely to be at least two orders of magnitude smaller, giving an average T_b at least 10^9 K. This lower limit to T_b strongly suggests, but does not prove, the maser nature of this emission.

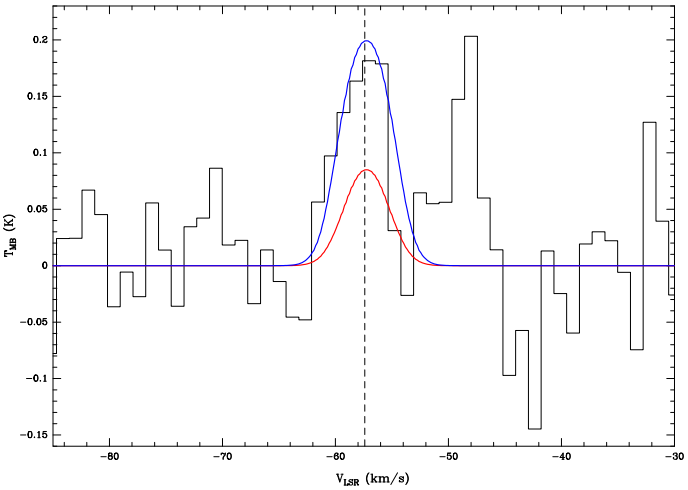

Fig. 7. SOFIA spectra of the o-H_2O $8_{2,7}-7_{3,4}$ line showing for feature (1) the best-fit thermal model in red from our HIFI data (see Fig. 6) and a model adopting a water inner abundance of 5.2×10^{-5} (blue profile).

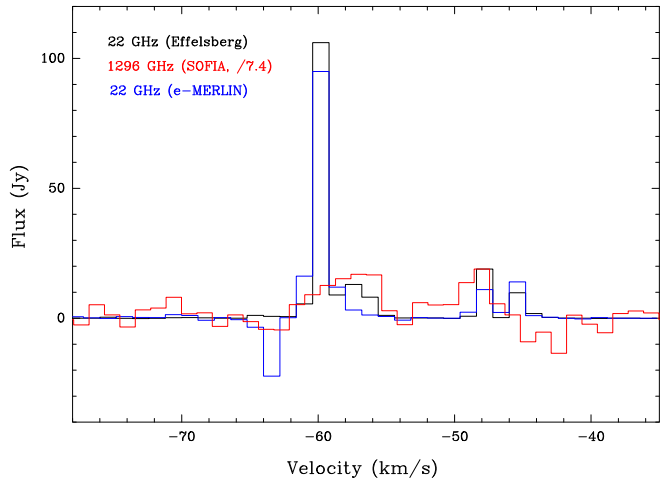

Fig. 8. As in Fig. 2, with all spectra smoothed to a spectral resolution of 1.1 km s^{-1}. The SOFIA fluxes have been divided by a factor 7.4.

Our conclusion is thus that the feature (2) water emission is likely a maser. The absence of the typical narrow substructure in the line profile could just be due to the low S/N (and spectral resolution) that hides it. Observations with some instrument that has much higher spatial resolution at 1296 GHz would be the only way to unambiguously prove it is a maser.

5. Discussion

5.1. Water content

Depending on the excitation of the o-H_2O $8_{2,7}-7_{3,4}$ line, purely thermal or not, we have shown that the water inner abundance might differ by more than one order of magnitude in the hot core of NGC 7538-IRS1. From the integrated fluxes measured for the lines (considered in this study) that are at least partly in emission, we derived the water luminosities and then estimated, assuming isotropic radiation, that the minimum total HIFI water luminosity is 0.6 $L_\odot$ (equal to the sum of all individual observed luminosities). Even though the true water emission from the inner parts might be much greater, the cool envelope absorbs much of the emission. This confirms the low contribution of water cooling to the total far-IR gas cooling compared to the cooling from other species (Karska et al. 2014; Herpin et al. 2016). Moreover, from the modeling, and assuming that the feature (1) water emission is purely thermal, we estimate the total water mass in the envelope to be 10^{-3} $M_\odot$ and that 93% of this mass resides in the inner parts, to be compared with 2×10^{-4} $M_\odot$ and 69% in the case of a nonthermal contribution.

5.2. Kinematics and geometry of the region

The previous section suggests that the THz water feature (1) is consistent with thermal excitation (even if a nonthermal contribution is possible), while feature (2) could be masing. Different physical conditions, that is, a different spatial origin, could explain these different behaviors. According to Gray et al. (2016), this could for instance be explained by a higher dust temperature in the region where the –57 km s^{-1} water is excited compared to the –48 km s^{-1} region (the o-H_2O $8_{2,7}-7_{3,4}$ inversion is lost with increasing dust temperature).

When we plot the 6.7 GHz methanol maser spots and the location of high-mass YSO IRS1a and b from Moscadelli & Goddi (2014) over our 22 GHz e-MERLIN map, the –48 km s^{-1} 22 GHz maser spots appear located close to the IRS1b source, while the –57 km s^{-1} spots are associated with the IRS1a source. Interestingly, Moscadelli & Goddi (2014), based on NH_3 maps, explain that the gas surrounding IRS1b (a less evolved source) has a lower temperature than the gas observed toward IRS1a, which is a more massive and evolved YSO, with T lower than 250 K. Hence, the higher temperature in IRS1a might be less suitable for water maser emission at 1296 GHz. It is more likely, however, that IRS1a could collisionally quench the maser if the number density is too high. We estimate the critical density (at T = 50 K) corresponding to the 1296 GHz transition to be 5×10^7 cm^{-3}. The gas in the core of IRS1a is thus so dense (number densities of up to a few 10^8 cm^{-3} can be reached in the inner part, see Sect. 4.2.1) that it begins to quench the maser action.

The maser spot distribution as derived from our e-MERLIN map provides new information when compared to previous published works. Figure 5 shows the spatial location of the 22 GHz maser features and the 6.7 GHz methanol masers of Moscadelli & Goddi (2014). According to these authors, the two individual high-mass YSOs, IRS1a and b, lie at the center of a line of methanol masers tracing disks with position angles of PA = +71° and −73°, respectively. The strongest "blue" (i.e., $v \leq -56$ km s^{-1}) maser spots we detect can be associated with IRS1a, others are distributed roughly along a line with PA = −25° and another with PA = −50°. Some similar linear distribution with PA = −52° was seen by Surcis et al. (2011), who suggested that these water masers were almost aligned with the CO NW-SE outflow, elongated 0.3 pc from IRS1a with PA = −40° (Kameya et al. 1990; Gaume et al. 1995; Qiu et al. 2011). They proposed that the water masers are pumped by a shock caused by the interaction of the outflow with the infalling gas (observed at scales ≥1000 AU, Beuther et al. 2013). The e-MERLIN map shows water masers following this NW-SE axis of the CO outflow, but at slower velocities compared to what Qiu et al. (2011) observed in CO (–78; –64 km s^{-1}). These H_2O maser spots might either trace the cavity of the outflow, that is, a cone with an opening angle of ∼25° and PA ≃ −40°, or trace two different outflows originating from IRS1a, the outflow at PA = −25° being almost perpendicular to the disk.

Maser spots whose velocity is close to the THz feature (2) (i.e., –44; –50 km s^{-1}) are located NW from IRS1a and W from IRS1b. They are also distributed along a line with PA ≃ +28°, that is, NE-SW, which can be associated with the outflow

observed by Beuther et al. (2013) in HCO^+(4-3) with PA $\simeq 40°$. Moreover, the NH_3 (Moscadelli & Goddi 2014), OCS, CH_3CN, and ^{13}CO (Zhu et al. 2013) observations show a velocity gradient in the same direction (PA $\sim$ 30–40°) with line emission at velocities similar to our feature (2) emission in this NE region. Moscadelli & Goddi (2014) explain these "redshifted" NH_3 features toward the NE by an outflow driven by IRS1b that is collimated by its rotating disk. Hence, as proposed above on the basis of a too high temperature toward IRS1a, we propose that the THz feature (2) is a maser, not associated with IRS1a, and is pumped by shocks that are driven by the IRS1b outflow.

6. Conclusions

SOFIA observations toward NGC 7538-IRS1 of the o-H_2O $8_{2,7}$–$7_{3,4}$ line emission were presented. Two separate velocity features were detected: one associated with the source velocity (–57.7 km s^{-1}), and another one lies at –48.4 km s^{-1}. By combining these observations with near-simultaneous observations of the $6_{1,6}$–$5_{2,3}$ masing transition of ortho-H_2O at 22 GHz with the Effelsberg telescope and with the e-MERLIN interferometer, we discussed the nature of these THz emission features.

A thermal water model based on HIFI observations can reproduce the $8_{2,7}$–$7_{3,4}$ line component at the source velocity if the water inner abundance is increased by more than an order of magnitude to 5.2×10^{-5} compared to what is estimated by the "HIFI alone" model. In addition, the observed brightness ratio (1296/22) for both features was compared to the maser predictions and led us to conclude that while the THz emission feature at the systemic velocity is mostly thermal, the –48.4 km s^{-1} feature is likely masing.

We argue that the two line components do not arise from the same location, meaning that different physical conditions could explain these different natures. The thermal emission is excited in the innermost part of the IRS1a protostellar massive object and is an excellent probe of the water reservoir in the inner part of the hot core. We suggest that the maser emission is associated with shocks driven by the IRS1b outflow.

Acknowledgements. We would like to thank Anne Lähteenmäki (Metsähovi Radio Observatory, Aalto University, Finland) for the flux measurements of 3C 84 and Alex Kraus (MPIfR-Bonn, Germany) for having performed and reduced the Effelsberg observations. The Effelsberg 100-m telescope is a facility of the MPIfR (Max-Planck-Institut für Radioastronomie) in Bonn. e-MERLIN is a national facility operated by The University of Manchester on behalf of the Science and Technology Facilities Council (STFC). We thank the SOFIA operations and the GREAT instrument teams, whose support has been essential for the GREAT accomplishments, and the DSI telescope engineering team. Based [in part] on observations made with the NASA/DLR Stratospheric Observatory for Infrared Astronomy. Sofia Science Mission operations are conducted jointly by the Universitis Space Research Association, Inc., under NASA contract NAS297001, and the Deutsches SOFIA Institut, under DLR contract 50 OK 0901. GREAT is a development by the MPI für Radioastronomie and the KOSMA/Universität zu Köln, in cooperation with the MPI für Sonnensystemforschung and the DLR Institut für Planetenforschung. *Herschel* is an ESA space observatory with science instruments provided by European-led Principal Investigator consortia and with important participation from NASA. HIFI has been designed and built by a consortium of institutes and university departments from across Europe, Canada and the United States under the leadership of SRON Netherlands Institute for Space Research, Groningen, The Netherlands and with major contributions from Germany, France and the US. Consortium members are: Canada: CSA, U.Waterloo; France: CESR, LAB, LERMA, IRAM; Germany: KOSMA, MPIfR, MPS; Ireland, NUI Maynooth; Italy: ASI, IFSI-INAF, Osservatorio Astrofisico di Arcetri- INAF; Netherlands: SRON, TUD; Poland: CAMK, CBK; Spain: Observatorio Astronómico Nacional (IGN), Centro de Astrobiología (CSIC-INTA). Sweden: Chalmers University of Technology – MC2, RSS & GARD; Onsala Space Observatory; Swedish National Space Board, Stockholm University – Stockholm Observatory; Switzerland: ETH Zurich, FHNW; USA: Caltech, JPL, NHSC.).

References

Aikawa, Y., Wakelam, V., Garrod, R. T., & Herbst, E. 2008, ApJ, 674, 984
Beuther, H., Leurini, S., Schilke, P., et al. 2007, A&A, 466, 1065
Beuther, H., Linz, H., & Henning, T. 2013, A&A, 558, A81
Chavarría, L., Herpin, F., Jacq, T., et al. 2010, A&A, 521, L37
Csengeri, T., Menten, K. M., Wyrowski, F., et al. 2012, A&A, 542, L8
Daniel, F., & Cernicharo, J. 2013, A&A, 553, A70
de Graauw, T., Helmich, F. P., Phillips, T. G., et al. 2010, A&A, 518, L6
Elitzur, M., Hollenbach, D. J., & McKee, C. F. 1992, ApJ, 394, 221
Felli, M., Brand, J., Cesaroni, R., et al. 2007, A&A, 476, 373
Fraser, H. J., Collings, M. P., McCoustra, M. R. S., & Williams, D. A. 2001, MNRAS, 327, 1165
Galván-Madrid, R., Montes, G., Ramírez, E. A., et al. 2010, ApJ, 713, 423
Gaume, R. A., Goss, W. M., Dickel, H. R., Wilson, T. L., & Johnston, K. J. 1995, ApJ, 438, 776
Gray, M. D., Baudry, A., Richards, A. M. S., et al. 2016, MNRAS, 456, 374
Herpin, F., Chavarría, L., van der Tak, F., et al. 2012, A&A, 542, A76
Herpin, F., Chavarría, L., Jacq, T., et al. 2016, A&A, 587, A139
Heyminck, S., Graf, U. U., Güsten, R., et al. 2012, A&A, 542, L1
Hogerheijde, M. R., & van der Tak, F. F. S. 2000, A&A, 362, 697
Kameya, O., Morita, K.-I., Kawabe, R., & Ishiguro, M. 1990, ApJ, 355, 562
Karska, A., Herpin, F., Bruderer, S., et al. 2014, A&A, 562, A45
Klein, B., Hochgürtel, S., Krämer, I., et al. 2012, A&A, 542, L3
König, C., Urquhart, J. S., Csengeri, T., et al. 2017, A&A, 599, A139
Minier, V., Booth, R. S., & Conway, J. E. 2000, A&A, 362, 1093
Moscadelli, L., & Goddi, C. 2014, A&A, 566, A150
Moscadelli, L., Reid, M. J., Menten, K. M., et al. 2009, ApJ, 693, 406
Neufeld, D. A., & Melnick, G. J. 1991, ApJ, 368, 215
Neufeld, D. A., Melnick, G. J., Kaufman, M. J., et al. 2017, ApJ, 843, 94
Ott, S. 2010, in Astronomical Data Analysis Software and Systems XIX, eds. Y. Mizumoto, K.-I. Morita, & M. Ohishi, ASP Conf. Ser., 434, 139
Qiu, K., Zhang, Q., & Menten, K. M. 2011, ApJ, 728, 6
Roelfsema, P. R., Helmich, F. P., Teyssier, D., et al. 2012, A&A, 537, A17
Sandell, G., Goss, W. M., Wright, M., & Corder, S. 2009, ApJ, 699, L31
Surcis, G., Vlemmings, W. H. T., Torres, R. M., van Langevelde, H. J., & Hutawarakorn, K., B. 2011, A&A, 533, A47
Thomas, H. S., & Fuller, G. A. 2008, A&A, 479, 751
van der Tak, F. F. S., van Dishoeck, E. F., Evans, II, N. J., & Blake, G. A. 2000, ApJ, 537, 283
van der Tak, F. F. S., Walmsley, C. M., Herpin, F., & Ceccarelli, C. 2006, A&A, 447, 1011
van der Tak, F. F. S., Chavarría, L., Herpin, F., et al. 2013, A&A, 554, A83
van Dishoeck, E. F., Kristensen, L. E., Benz, A. O., et al. 2011, PASP, 123, 138
Werner, M. W., Becklin, E. E., Gatley, I., et al. 1979, MNRAS, 188, 463
Wilson, T. L., & Rood, R. 1994, ARA&A, 32, 191
Yates, J. A., Field, D., & Gray, M. D. 1997, MNRAS, 285, 303
Young, E. T., Becklin, E. E., Marcum, P. M., et al. 2012, ApJ, 749, L17
Zhu, L., Zhao, J.-H., Wright, M. C. H., et al. 2013, ApJ, 779, 51

Appendix A: Water line transitions observed with *Herschel*/HIFI

Table A.1. Water line transitions observed with *Herschel*/HIFI.

Water species	Frequency [GHz]	Wavelength [μm]	E_u [K]	HIFI band	Beam [$''$]	$\eta_{\rm mb}$	$T_{\rm sys}$ [K]	rms [mK]	Obsid
o-$H_2^{18}O$ 1_{10}–1_{01} [a]	547.6764	547.4	60.5	1a	37.8	0.62	80	58	1342202036
o-$H_2^{17}O$ 1_{10}–1_{01}	552.0209	543.1	61.0	1a	37.8	0.62	70	42	1342198332-3
p-$H_2^{18}O$ 2_{02}–1_{11}	994.6751	301.4	100.6	4a	21.1	0.63	290	69	1342197964-5
o-$H_2^{18}O$ 3_{12}–3_{03}	1095.6274	273.8	248.7	4b	19.9	0.63	380	48	1342200760-1
p-$H_2^{18}O$ 1_{11}–0_{00}	1101.6982	272.1	52.9	4b	19.9	0.63	390	36	1342191663-4, 1342197976
p-$H_2^{17}O$ 1_{11}–0_{00}	1107.1669	272.1	52.9	4b	19.9	0.63	380	37	1342200760-1
o-$H_2^{17}O$ 2_{12}–1_{01}	1662.4644	180.3	113.6	6b	12.7	0.58	1410	232	1342200758
o-H_2O 1_{10}–1_{01} [a]	556.9361	538.3	61.0	1a	37.1	0.62	80	65	1342202036
p-H_2O 2_{11}–2_{02}	752.0332	398.6	136.9	2b	28.0	0.64	90	67	1342201546-7
p-H_2O 5_{24}–4_{31} [b]	970.3150	309.0	598.8	4a	21.8	0.63	620	59	1342227536
p-H_2O 2_{02}–1_{11}	987.9268	303.5	100.8	4a	21.3	0.63	340	69	1342197964-5
o-H_2O 3_{12}–3_{03}	1097.3651	273.2	249.4	4b	19.9	0.63	380	49	1342200760-1
p-H_2O 1_{11}–0_{00}	1113.3430	269.0	53.4	4b	19.7	0.63	395	36	1342191663-4, 1342197976
o-H_2O 2_{21}–2_{12}	1661.0076	180.5	194.1	6b	12.7	0.58	1410	232	1342200758
o-H_2O 2_{12}–1_{01}	1669.9048	179.5	114.4	6b	12.6	0.58	1410	232	1342200758

Notes. The rms is the noise in $\delta\nu$ = 1.1 MHz. [(a)] This line was mapped in OTF mode. [(b)] Line affected by strong baseline and ripple problems.

Appendix B: Water maser positions

Table B.1. Water maser positions and velocities at 22 GHz (e-MERLIN observations of April 2016).

IRS	Group	offset X[a]	Offset Y[a]	Peak S_ν	Peak V_{LSR}	Velocity range
		[″]	[″]	[Jy]	[km s^{-1}]	[km s^{-1}]
1	1	0.132	–0.010	17.31	–45.06	–44.64 to –45.70
1	2	0.133	0.005	143.23	–45.27	–44.43 to –45.91
1	3	0.070	–0.106	13.12	–48.33	–48.22 to –48.65
1	4	0.0762	–0.095	145.27	–48.12	–47.49 to –48.96
1	5	0.114	–0.081	4.21	–48.12	–48.12 to –48.54
1	6	0.114	–0.061	4.61	–48.22	–48.12 to –48.64
1	7	0.123	–0.060	1.01	–48.12	–48.12 to –48.33
1	8	0.079	–0.070	2.91	–48.33	–48.33 to –48.75
1	9	–0.001	–0.122	9.16	–54.96	–54.44 to –55.49
1	10	–0.042	–0.160	23.23	–57.91	–56.54 to –57.91
1	11	–0.288	–0.010	29.24	–58.23	–57.81 to –58.55
1	12	–0.287	–0.012	62.02	–58.34	–57.81 to –59.07
1	13	–0.278	–0.037	2.92	–58.12	–58.12 to –58.34
1	14	–0.304	–0.051	1.44	–58.34	–58.34 to –58.65
1	15	–0.251	–0.027	0.86	–58.65	–58.44 to –58.65
1	16	–0.238	0.012	1.88	–58.44	–58.44 to –58.65
1	17	0.094	0.038	8.59	–59.28	–58.86 to –59.49
1	18	0.005	–0.250	112.31	–60.13	–59.92 to –60.65
1	19	0.006	–0.234	29.61	–60.23	–60.13 to –60.44
1	20	–0.012	–0.258	26.90	–60.55	–60.13 to –60.55
1	21	0.004	–0.250	964.41	–60.01	–59.18 to –61.07
1	22	0.020	–0.2820	10.34	–59.81	–59.39 to –59.81
1	23	–0.018	–0.195	12.34	–59.70	–59.39 to –59.81
1	24	0.036	–0.319	6.97	–59.70	–59.39 to –59.81
1	25	0.048	–0.243	6.46	–60.76	–60.55 to –61.07
1	26	–0.111	–0.154	27.73	–61.39	–60.86 to –62.23
1S	1	–0.163	–1.201	14.32	–70.66	–69.20 to –70.98
1S	2	–0.170	–1.211	27.09	–46.43	–45.80 to –47.07
3	1	–5.647	2.456	14.40	–56.86	–56.33 to –57.60
3	2	–5.642	2.474	88.55	–56.76	–56.12 to –57.91
9	1	117.433	–50.752	2.06	–69.18	–68.97 to –69.19
9	2	117.432	–50.751	2.76	–69.39	–69.39 to –69.61
9	3	117.436	–50.742	39.13	–73.61	–72.45 to –74.98
11	1	–2.747	–80.919	7.56	–44.96	–44.75 to –45.70
11	2	–2.736	–80.885	32.20	–45.48	–45.27 to –45.60
11	3	–2.743	–80.926	29.41	–47.06	–45.91 to –47.80
11	4	–2.733	–80.888	12.24	–46.75	–46.33 to –47.60
11	5	–2.748	–80.970	2.38	–47.28	–46.85 to –47.49
11	6	–2.738	–80.984	6.84	–47.06	–46.64 to –47.59
11	7	–2.730	–80.846	2.83	–46.85	–46.64 to –47.17
11	8	–2.715	–80.960	1.82	–46.85	–46.65 to –47.06
11	9	–2.684	–80.908	2.05	–47.38	–47.17 to –47.38
11	10	–4.127	–79.095	9.53	–50.01	–49.59 to –50.33
11	11	–4.112	–79.057	5.23	–49.59	–49.59 to –50.22
11	12	–4.116	–79.160	3.88	–50.12	–49.91 to –50.22
11	13	–4.123	–79.126	1.69	–50.44	–50.22 to –50.44
11	14	–4.300	–80.046	3.94	–53.49	–53.28 to –53.81
11	15	–4.293	–80.012	1.64	–53.81	–53.38 to –53.81
11	16	–2.928	–81.067	21.02	–54.12	–53.81 to –54.65
11	17	–2.918	–81.120	11.80	–54.44 –	53.91 to –54.65
11	18	–2.931	–80.992	5.31	–54.23	–53.91 to –54.44
11	19	–2.919	–81.039	3.24	–54.23	–53.91 to –54.44
11	20	–2.874	–81.056	2.21	–54.33	–54.33 to –54.54
11	21	–2.793	–80.885	4.52	–55.60	–55.07 to –55.70

Notes. [(a)] All offsets are relative to the position RA = 23h13m45.364s, Dec = +61°28′10.550″). The uncertainty is smaller than 0.003″.

Table B.1. continued.

IRS	Group	offset X[a]	offset Y[a]	Peak S_ν	Peak V_{LSR}	Velocity range
		[″]	[″]	[Jy]	[km s^{-1}]	[km s^{-1}]
11	22	–2.784	–80.861	2.92	–55.28	–55.07 to –55.49
11	23	–2.914	–81.168	1.77	–55.81	–55.81 to –56.02
11	24	–1.121	–81.967	10.40	–56.02	–55.91 to –57.97
11	25	–1.112	–81.940	1.90	–56.23	–56.23 to –56.65
11	26	–4.594	–79.578	10.02	–57.07	–56.22 to –57.18
11	27	–2.797	–80.876	19.98	–57.07	–56.33 to –57.49
11	28	–2.871	–81.223	2.77	–56.44	–56.44 to –56.97
11	29	–2.882	–81.287	3.08	–56.97	–56.97 to –57.39
11	30	–2.879	–81.252	20.05	–56.97	–56.44 to –57.49
11	31	–2.839	–81.272	4.61	–56.86	–56.54 to –56.97
11	32	–2.787	–80.850	7.56	–57.18	–56.65 to –57.39
11	33	–2.761	–80.925	3.04	–56.97	–56.65 to –56.97
11	34	–2.970	–80.858	11.43	–57.81	–56.97 to –57.81
11	35	–2.763	–80.905	3.31	–57.07	–57.07 to –57.28
11	36	–2.789	–80.938	2.40	–57.28	–57.07 to –57.28
11	37	–2.840	–81.266	2.72	–57.07	–57.07 to –57.28
11	38	–2.952	–80.824	3.21	–57.28	–57.28 to –57.70
11	39	–4.240	–79.974	81.11	–58.02	–57.49 to –58.76
11	40	–4.212	–80.030	38.97	–57.91	–57.60 to –58.23
11	41	–4.222	–79.902	22.69	–58.02	–57.60 to –58.55
11	42	–4.227	–79.945	36.30	–58.02	–57.70 to –58.55
11	43	–4.173	–79.965	22.74	–58.23	–57.81 to –58.44
11	44	–4.233	–80.036	13.97	–58.23	–58.12 to –58.65
11	45	–4.242	–80.017	34.93	–58.34	–57.91 to –58.76
11	46	–4.303	–79.883	15.34	–58.02	–57.91 to –58.34
11	47	–3.068	–80.774	28.26	–60.23	–59.92 to –60.76
11	48	–3.055	–80.732	15.82	–60.34	–60.13 to –60.44
11	49	–3.038	–80.696	9.06	–60.34	–60.34 to –60.55
11	50	–3.123	–80.708	5.96	–61.81	–61.49 to –62.02
11	51	–3.115	–80.665	2.34	–61.71	–61.60 to –61.92
11	52	–3.172	–80.408	1.77	–62.23	–62.23 to –62.55
11	53	–3.162	–80.369	2.63	–62.23	–62.23 to –62.55
11	54	–2.800	–80.898	50.61	–63.81	–63.71 to –64.34
11	55	–2.802	–80.879	245.82	–63.39	–62.44 to –64.44
11	56	–2.791	–80.843	221.66	–63.18	–62.44 to –65.08
11	57	–2.767	–80.918	114.46	–63.18	–62.65 to –63.19
11	58	–2.826	–80.779	22.41	–63.18	–62.76 to –63.29
11	59	–2.783	–80.800	54.47	–63.39	–62.86 to –63.71
11	60	–2.791	–80.934	159.10	–63.30	–62.76 to –64.13
11	61	–2.877	–80.791	107.47	–63.60	–62.86 to –64.02
11	62	–2.734	–80.850	3.92	–63.30	–63.39 to –63.60
11	63	–2.734	–80.857	128.98	–63.39	–62.97 to –64.02
11	64	–3.175	–80.372	50.63	–63.50	–63.39 to –64.87
11	65	–3.177	–80.414	25.18	–64.04	–63.60 to –64.55
11	66	–2.775	–80.799	3.42	–63.92	–63.92 to –64.13
11	67	–3.165	–80.336	5.61	–64.34	–64.13 to –64.76
11	68	–2.778	–80.815	2.26	–64.34	–64.23 to –64.66
New	1	–11.957	–21.192	19.79	–46.12	–45.17 to –47.06
New	2	–11.960	–21.199	3.81	–52.96	–52.75 to –53.28
New	3	–11.980	–21.215	8.31	–56.12	–55.49 to –56.86
New	4	–13.992	–23.778	28.29	–57.81	–57.07 to –58.02
New	5	–13.989	–23.756	198.18	–57.60	–56.33 to –59.49
New	6	–13.964	–23.785	2.68	–56.97	–56.65 to –56.97
New	7	–11.997	–21.222	35.84	–63.39	–61.39 to –63.39